

Endothelial Leakiness Induced by Amyloid Protein Aggregation

Yuhuan Li

Fudan University <https://orcid.org/0000-0002-1191-0793>

Nengyi Ni

National University of Singapore

Myeongsang Lee

Clemson University <https://orcid.org/0000-0003-2078-6023>

Wei Wei

Southwest University

Nikolaos Andrikopoulos

Monash Institute of Pharmaceutical Sciences

Aleksandr Kakinen

University of Queensland <https://orcid.org/0000-0003-1547-2855>

Thomas P Davis

Australian Institute for Bioengineering and Nanotechnology, The University of Queensland,

Yang Song

Chinese Academy of Sciences <https://orcid.org/0000-0001-7716-9216>

Feng Ding

Clemson University <https://orcid.org/0000-0003-1850-6336>

David Leong (✉ cheltwd@nus.edu.sg)

National University of Singapore <https://orcid.org/0000-0001-8539-9062>

Pu Chun Ke

Monash University <https://orcid.org/0000-0003-2134-0859>

Article

Keywords: endothelial leakiness, VE cadherin, amyloid protein, APEL, discrete molecular dynamics simulation, nanoparticulate

Posted Date: January 19th, 2022

DOI: <https://doi.org/10.21203/rs.3.rs-1161788/v1>

License:  This work is licensed under a Creative Commons Attribution 4.0 International License.

[Read Full License](#)

Abstract

Alzheimer's disease (AD) is a major cause of dementia debilitating the global ageing population. Current understanding of the AD pathophysiology implicates the aggregation of amyloid beta (A β) as causative to neurodegeneration, with tauopathies and neuroinflammation considered as other major culprits. Curiously, vascular endothelial barrier dysfunction is strongly associated with A β deposition and 80-90% AD subjects also experience cerebral amyloid angiopathy. Here we show amyloid proteins-induced endothelial leakiness (APEL) in human microvascular endothelial monolayers as well as in mouse cerebral vasculature. Using signaling pathway assays and discrete molecular dynamics, we revealed that the angiopathy first arose from a disruption to vascular endothelial (VE)-cadherin junctions exposed to the nanoparticulates of A β oligomers and seeds, preceding the earlier implicated proinflammatory and pro-oxidative stressors to endothelial leakiness. These findings are analogous to nanomaterials-induced endothelial leakiness (NanoEL), a major phenomenon in nanomedicine depicting the paracellular transport of anionic inorganic nanoparticles in the vasculature. As APEL also occurred with the anionic seeds of pathogenic alpha synuclein and functional FapC bacterial amyloid, this study projects a general new paradigm for elucidating the vascular permeation, systemic spread, and cross-seeding of amyloid proteins that underlie the pathogeneses of AD, Parkinson's, as well as a range of amyloid diseases.

1. Introduction

Alzheimer's disease (AD) is a primary form of neurological disorder entailing severe adverse effects on the memory, cognition, and life expectancy of the global ageing population. The most influential paradigm concerning the AD pathology is the amyloid cascade hypothesis proposed by Hardy and Higgins in 1992¹ and its modifications thereafter, where amyloid beta (A β) evolves from disordered monomers to toxic oligomers and amyloid fibrils through molecular self-assembly, modulated by environmental factors such as pH, temperature, metals, chaperones, and cell membranes². Accordingly, much effort over the past three decades has been made towards inhibiting or clearing the toxic A β aggregates, employing small molecules, peptidomimetics, antibodies and, more recently, nanoparticles³⁻¹². A lack of clinical success, however, has shrouded these efforts suggesting the pathophysiology of AD is multifactorial as its triggers¹³.

Indeed, it has now been realized that, in addition to A β amyloidogenesis, tauopathies, apolipoprotein E, and neuroimmune activation are all causative to neurodegeneration in AD¹³. The great (80-90%) correlation between AD subjects and patients carrying cerebral amyloid angiopathy (CAA) further suggests an important role of endothelial integrity in the development of AD pathogenesis¹⁴, also evidenced by observations of cerebral endothelial dysfunction and microvascular injury induced by A β ¹⁵⁻¹⁷. Intriguingly, while A β originates from the proteolytic cleavage of amyloid precursor protein (APP) in endosomal membrane¹⁸, deposits of A β are seen throughout the central nervous system, cerebral blood vessels, cerebrospinal fluid, and the plasma^{14,19,20}. A β -mediated vasoactivity, vascular capillary constriction, blood flow reduction, and paracellular transport have been reported with endothelial

monolayers, blood-brain barrier (BBB), and biopsied human and rodent brain tissues^{15,17,21–23}, in connection with the production of reactive oxygen species (ROS), modified cytoskeletal network, altered tight-junction protein expression, and signaling to pericytes.

In this study, we report on amyloid proteins-induced endothelial leakiness (APEL) in human microvascular endothelial cell (HMVEC) monolayers resulting from their exposure to the nanoparticulates of oligomers, protofibrils, and sonicated amyloid seeds of A β ₄₂ (abbreviated as “seeds” and “A β ” hereafter), Parkinson’s alpha synuclein (abbreviated as “ α S” hereafter) and FapC, a major protein constituent of the extracellular functional amyloid matrix of *Pseudomonas aeruginosa*. We further demonstrated endothelial leakiness *in vivo* with mouse cerebral vasculature exposed to A β oligomers and seeds. Using signaling pathway assays and steered discrete molecular dynamics (sDMD) simulations, we revealed that APEL arose from the anionic protein nanoparticulates interacting with vascular endothelial (VE)-cadherins and their associated adherens junction machinery. Our *in vitro* data showed that APEL arose from non-ROS and non-apoptotic events, where A β oligomers and seeds instead underwent direct extracellular interactions with VE-cadherins to trigger molecular pathways yielding intercellular gap formation. Through the sDMD simulations, we found that the oligomers remarkably reduced the cadherin dimer stability followed by the amyloid seeds, while flexible amyloid monomers did not affect the cadherin integrity. These results converged on a general new phenomenon that the nanoparticulates of anionic peptides and proteins rendered through molecular self-assembly and fragmentation, can remodel the vasculature endothelium preceding the onset of ROS, inflammation, cytotoxicity, and cerebral blood flow constriction as suggested by earlier etiological paradigms^{16,21,23–26}.

Phenomenologically as well as mechanistically, APEL is analogous to nanomaterials-induced endothelial leakiness (NanoEL)^{27–29}, where in the latter, anionic inorganic nanoparticles of less than 100 nm in size open up the endothelial paracellular route by disrupting the VE-cadherin junctions of apposing cells. The observed occurrence of APEL here was highly surprising in that proteins and peptides are biomolecules differing significantly from inorganic nanoparticles in origin, structure and function, and the density of proteins/peptides (\sim 1.35 g/m³) is markedly below the density threshold determined for NanoEL-competent inorganic nanoparticles (1.72 g/m³)³⁰. Regardless, the findings of APEL entailed rich biological and medical implications, from the systemic spread of amyloid proteins to their cross-seeding, BBB translocation, and clearance that underpin the pathogeneses of AD, Parkinson’s disease (PD) and other amyloid diseases debilitating the brain and other human organs.

2. Results And Discussion

2.1 Characterization of amyloid protein aggregates

In our previous works^{27,31}, we found that certain nanoscale structures could interact with the VE-cadherin proteins in adherens junctions, leading to a cascade of intracellular signaling that included actin rearrangements and development of transient intercellular gaps – a phenomenon we termed as NanoEL.

Although our previously used nanoparticles were synthetic and not of a natural origin, the current evidence reiterated that it was their possession of certain physicochemical traits, such as their size range³¹ and anionic charge³² that conferred them with the NanoEL ability, instead of their identity as being a certain material. Considering this, we hypothesized that biological nanoparticulates such as amyloid protein aggregates possessing an optimal size range, stiffness and anionic charge, could potentially induce a similar phenomenon to NanoEL when interacting with the endothelium. A β (isoelectric point pl: 5.5)³³ oligomers and seeds were first chosen due to their relevance in vascular pathology and their significance to AD, as well as their polymorphic architectures. Three other types of amyloid proteins were also employed to facilitate a comprehensive understanding of APEL with respect to protein composition, size, and charge. aS, an anionic neuronal protein (pl: 4.67)³⁴ implicated in the pathology of PD^{35,36}, islet amyloid polypeptide (IAPP), a cationic pancreatic polypeptide (pl: 8.8)³⁷ implicated in the pathology of type 2 diabetes (T2D)³⁸, and FapC, an anionic protein of *Pseudomonas aeruginosa* functional amyloid, were used in our study³⁹.

Fibrillization of the four amyloid protein species was performed (described within **Experimental Section**) and a thioflavin T (ThT) fluorescence kinetic assay was conducted simultaneously to monitor the amyloid formation processes. Samples at various time points were analyzed via transmission electron microscopy (TEM) to confirm their structural evolution. In Figure 1B, TEM images depicted 6 distinctly different structures of A β , obtained at 0 h ($A\beta_m$), 5h ($A\beta_o$), 8 h ($A\beta_{o-p1}$), 12 h ($A\beta_{o-p2}$) and 24 h ($A\beta_f$ and $A\beta_s$), respectively, where $A\beta_f$ denoted mature fibrils and $A\beta_s$ sonicated fibril fragments. Similar monomers, oligomers, mature fibrils, and sonicated seeds were imaged for aS, IAPP and FapC (Figure 1C to E). Subsequently, different aggregation structures of each amyloid protein were prepared according to the time points of 0 h (aS_m), 20 h (aS_o) and 96 h (aS_f and aS_s) for aS, 0 h ($IAPP_m$), 1 h ($IAPP_o$) and 24 h ($IAPP_f$ and $IAPP_s$) for IAPP, and 180 h for FapC_s according to their ThT assays (Figure 1F). In Figure 1G, the sizes of the various amyloid protein aggregates were tabulated from the TEM analysis, where the oligomers of the four amyloid proteins ranged ~20-70 nm in length and their seeds ~20-90 nm in length, with their thicknesses below 20 nm.

2.2 APEL was observed with several species of amyloid protein aggregates

Subsequently, we investigated the occurrence of endothelial leakiness when HMVECs were treated for 30 min with varied sizes of A β (monomers $A\beta_m$, oligomers $A\beta_o$, protofibrils $A\beta_{o-p1}$ and $A\beta_{o-p2}$, fibrils $A\beta_f$ and sonicated seeds $A\beta_s$), aS (monomers aS_m , oligomers aS_o and seeds aS_s), IAPP (monomers $IAPP_m$, oligomers $IAPP_o$ and seeds $IAPP_s$), and FapC (seeds FapC_s). Confocal fluorescence microscopy revealed APEL occurring in the endothelial cell monolayers exposed to the protein nanoparticulates (Figure 2A and B). Notably, IAPP, the only positively charged peptide, did not induce any leakiness in endothelial barrier across all its four forms, including the seeds, which led to leakiness for all other three types of amyloid protein aggregates. This suggested that the characteristic of negative charge, as opposed to positive charge, is a necessary factor for the APEL phenomenon to occur. Within the three anionic amyloid species

that gave rise to APEL, their soluble monomers and lengthy amyloid fibrils were unable to induce leakiness.

Gap area, diameter, and frequency distribution were analyzed from captured images (Figure 2C and S1, **Table S1**). In Figure 2C, for the forms of A β , the calculated percentage of gap area was insignificant for A β_m when compared to the non-leaky control, followed by a significant increase for A β_o , before decreasing when the aggregate length increased from A β_{o-p1} to A β_f , where gap area % finally became insignificant compared to control. The subsequent sonication of A β_f to A β_s led to a significant APEL occurrence again. In frequency distribution, the number of gaps induced by A β_o was $14.3 \pm 3.1 \times 10^2$ gaps/mm 2 , which decreased to $5.3 \pm 2.8 \times 10^2$ gaps/mm 2 for A β_{o-p2} and increased back to $15.8 \pm 6.8 \times 10^2$ gaps/mm 2 after A β_s were introduced (**Figure S1**). Similarly, aS $_o$ and aS $_s$ yielded significant increases in gap formation, while aS $_m$ did not elicit leakiness of significance against untreated control (Figure 2C, S1). Functional FapC $_s$, tested solely as seeds, also elicited significant gap formation. Next, we employed transwell assays to quantify the extent of induced endothelial leakiness with the use of fluorescein isothiocyanate conjugated dextran (FITC-dextran) as a probe. In agreement with confocal fluorescence microscopy, the transwell assay revealed that when the four forms of A β (A β_m , A β_o , A β_f , A β_s) were incubated with HMVECs and probed for permeability changes, there were significant increases in FITC-dextran transport across the endothelial barrier for A β_o and A β_s compared to untreated control, while A β_m and A β_f did not yield significant results (Figure 2D).

Collectively, APEL bore similarities with NanoEL. The differing identities of the amyloid species (such as human or bacterial origin, pathogenic or functional) did not appear to dictate the occurrence of APEL on endothelial barriers, but rather possession of relevant physicochemical properties, such as suitable size range and negative charge, was necessary. Better performances by the oligomers and sonicated A β seeds than fibrils, along with the short duration of induction (30 min, or likely even faster) in increasing vascular permeability were notable as APEL differed from some currently proposed mechanisms of A β -induced permeability. These include: rat brain microvessel endothelial cells subjected to fibrillar A β_{42} for durations of 24-72 h exhibited an altered pattern of tight junction protein expression and localization⁴⁰; murine brain endothelial cells subjected to A β_{42} for 24 h led to increased permeability, which was proposed to result from A β_m interacting with receptors for advanced glycation end products (RAGE), leading to downstream disturbance to tight junction protein expression and permeabilization⁴¹; and human umbilical vein endothelial cell barrier treated with A β_{42} for 24 h experienced downregulated junction protein expression and increased permeability⁴². Hence, we were prompted to further elucidate the specifics of the APEL process.

2.3 *In vitro* A β APEL occurs independently of toxicity phenomena or endocytic process

We isolated one species of the amyloid proteins that resulted in significant APEL, A β , for subsequent characterization of the APEL process. The two forms that induced the most significant fold changes in

leakiness (Figure 2D), A β _o and A β _s, were identified and selected. A β -induced APEL was first characterized through a transwell assay, where HMVECs were treated with A β _o and A β _s at two concentrations (20 μ M and 40 μ M) for 30 min. We measured an increase in FITC-dextran transport (and therefore, leakiness) with increasing concentrations of both A β forms (Figure 3A). Next, these APEL-relevant concentrations of A β were employed in examination of common toxicity effects that could lead to intercellular gap formation, which were important due to A β 's established roles in neurotoxicity when interacting with brain endothelial cells¹. ROS is known to lead to cell shrinkage through apoptosis⁴³, and free radical oxidative stress is a critical pathological effect by A β ^{44,45}. We detected no significant increase in ROS production under the different A β treatments for as late as 2 h, beyond the timepoint (30 min) when APEL had occurred (Figure 3B). In complement, as seen in Figure 3C, prior treatment with ROS scavenger N-acetyl cysteine (NAC) did not significantly reduce the degree of A β -induced APEL despite ROS scavengers being reported as protective against A β -induced oxidative stress⁴⁶. In addition, apoptosis, a known contributor to cell shrinkage⁴⁷, was also reported as a toxic effect induced by A β structures from oligomers to fibrils, involving caspases such as 3, 8 and 9^{48–50}. Firstly, no decline in cell viability was detected under A β -induced APEL conditions (Figure 3D). Subsequently, as shown in Figure 3E, we detected no activated forms of important apoptotic enzymes, namely caspase 9 (an initiator caspase), caspase 3 (an effector caspase), and poly(ADP-ribose) polymerase (PARP; a downstream cleavage target) during A β -induced APEL conditions^{51,52}. Furthermore, endocytosis was found to not significantly contribute to A β -induced APEL as the mixture of endocytic inhibitors methyl- β -cyclodextrin (M β CD) and monodansylcadaverine (MDC) could not significantly reduce leakiness induced in the HMVEC barrier (Figure 3F). Collectively, A β -induced APEL was found to be not significantly attributable to endothelial toxic effects typical to A β , most likely due to the short duration (30 min) of cell exposure to A β , and was triggered extracellularly, bearing strong similarities to NanoEL⁵³.

2.4 *In vitro* A β -induced APEL involves extracellular interactions with VE-cadherin

To validate the extracellular triggering of the APEL process and potential involvement of interactions of A β with adherens junction protein VE-cadherin, we further performed a competitive inhibition assay with A β _s. A pre-treatment of BV-6 antibody blocked the extracellular domain of VE-cadherin before the later incubation with A β _s. Concurrently, a similar set of groups instead involving pre-treatment with NAC was employed. NAC was a pre-treatment not anticipated to decrease the overall APEL extent, based on our findings in Figure 3B and C. As captured in confocal fluorescence microscopy in Figure 4A and then analyzed semi-quantitatively in Figure 4B, the percentage of gap area formation was significantly reduced under the additional BV-6 pre-treatment (BV-6+A β _s) compared to only A β _s. Interestingly, only adding BV-6 also led to some significant gap formation in HMVEC monolayers compared against the untreated control. However, it is important to note that there were no significant differences between BV-6+A β _s group and only BV-6 group, which suggested BV-6 had negated the effects exerted by A β _s. Taken together, extracellular interactions with VE-cadherin were not only important but essential for the

occurrence of APEL. In the parallel series, the degree of gap formation under $\text{A}\beta_s$ was not significantly reduced by pre-treatment with NAC. Comparison between control, NAC-only and NAC+ $\text{A}\beta_s$ groups affirmed that NAC played no role in inducing APEL and the APEL effect was exerted by $\text{A}\beta_s$. Gap frequency distribution analysis (**Figure S2**) supported similar overall conclusions. The $\text{A}\beta_s$ -only group had a frequency of $21.7 \pm 2.4 \times 10^2$ gaps/mm², while BV-6 + $\text{A}\beta_s$ exhibited a significant decrease in gap frequency with $10.3 \pm 5.0 \times 10^2$ gaps/mm². As anticipated, NAC+ $\text{A}\beta_s$ group yielded no significant decrease in gap frequency compared to $\text{A}\beta_s$ -only group, at $18.7 \pm 5.3 \times 10^2$ gaps/mm².

Next, we employed a co-localization assay where cells were treated with ThT-labeled $\text{A}\beta_s$ and VE-cadherin was later labeled during immunofluorescence staining. Under confocal fluorescence microscopy, it was observed that bright yellow dots were yielded, indicating ThT-labeled $\text{A}\beta_s$ (in green channel) and high VE-cadherin expression levels (in red channel) were co-localized (Figure 4C). The yellow dots were located along the perimeters of HMVECs, where the cell junctions were found, and most were just next to or inside the intercellular gaps. This assay further suggested that interactions took place between $\text{A}\beta_s$ and VE-cadherins during the APEL process.

2.5 *In vitro* $\text{A}\beta$ -induced APEL involves VE-cadherin signaling and actin remodeling

To further elucidate the molecular mechanisms behind $\text{A}\beta$ -induced APEL, we examined the effects of APEL on VE-cadherin signaling pathway. Canonically, VE-cadherin signaling includes phosphorylation at two important residues tyrosine 658 (Y658) and tyrosine 731 (Y731), which leads to downstream reduced interactions with p120 and β -catenin, with actin rearrangement and appearance of intercellular retractions as notable endpoints^{54–57}. Our previous works with NanoEL revealed that a similar cascade could also be triggered by synthetic nanoparticles with certain physicochemical parameters, despite their exogenous origin^{31,53}. In a similar manner, we observed increased phosphorylation of Y658 and Y731 residues of VE-cadherin under $\text{A}\beta_o$ treatment, where the degree of phosphorylation increased with the concentration of $\text{A}\beta$ (Figure 5A). Src-kinase inhibitor, PP1, which inhibits the kinase responsible for phosphorylation of the residues, was also employed as a pre-treatment, where it was observed that the degree of phosphorylation under every $\text{A}\beta_o$ treatment decreased compared to their relevant control but was incompletely inhibited (Figure 5A-C). Likewise, $\text{A}\beta_s$ treatment resulted in increased phosphorylation of the two residues and application of PP1 pre-treatment modulated an increase in phosphorylation (Figure 5D-F). Complementarily, in our parallel transwell assay, PP1 pre-treatment also resulted in a significant reduction of induced leakiness under the treatment of either $\text{A}\beta$ nanoparticulates, when compared to their non-PP1 pre-treated counterparts (Figure 5E). This further evidenced the involvement of activated VE-cadherin signaling during the APEL phenomenon. To validate the involvement of actin remodeling in the APEL event, we also employed a Rho-associated, coiled-coil containing protein kinase (ROCK) inhibitor, Y27632, which disrupts normal actin functioning through destabilizing focal adhesions and stress fibers⁵⁸. The transwell assay revealed that pre-treatment with Y27632, which interfered with normal actin

remodeling, led to suppressed induction of leakiness by A β _o or A β _s compared to the respective untreated groups (Figure 5F). Together, these results revealed the role of VE-cadherin signaling and actin remodeling as part of the molecular mechanisms involved during APEL.

2.6 A β -induced APEL with *ex vivo* blood vessels and *in vitro*& *in vivo* BBB models

In addition to *in vitro* investigation, an *ex vivo* assay was further conducted to determine vascular leakiness in swine vessels after the treatment of A β _o or A β _s at 200 or 400 μ M (Figure 6A, B). Permeability of Evans blue dye (EBD) at concentrations of 200 μ M and 400 μ M for both A β species had a significant increase compared to the respective untreated control. The highest degree of permeabilization was observed at 400 μ M for both species. Subsequently, the A β species were investigated for their effects on the permeability of the BBB. Human brain endothelial cells hCMEC/D3 were employed as a BBB model in the transwell assay format and exposed to 0-40 μ M of A β _s. An increase in the penetration of FITC-dextran was observed with increasing concentration of A β _s, with 40 μ M of A β _s attaining the highest permeability compared to control of 0 μ M, while 5 μ M had a comparatively insignificant difference (Figure 6C). Considering the significant induction of permeability by A β species in the *in vitro* BBB model, we further determined the effects of A β in an *in vivo* setting. Swiss mice were intravenously injected with a solution of EBD containing either A β _s or A β _o, or solely EBD. Fluorescence imaging of mice brains post-sacrifice revealed increased the permeability across BBB for both A β _s and A β _o treatments compared to EBD-only treatment, with the A β _s group attaining the higher increase in permeability (Figure 6D). Furthermore, transverse brain sections were also derived from mice after similar injected treatments for immunofluorescence analysis after staining with anti-A11 antibody (Figure 6E). Presence of A β structures resembling oligomers were found in both A β _s and A β _o groups, as inferred from the anti-A11 antibody staining. Comparatively, no A β structures were discovered in the EBD-only treated control. Together, the *in vivo* findings revealed an increased permeability in the brains of mice after treatment with A β species, as corroborated by a concurrent presence of A β structures within brains.

2.7 A β interactions with VE-cadherin dimers characterized *in silico*

To understand the disruption of VE-cadherin dimer induced by amyloid proteins at the molecular level, we employed all-atom discrete molecular dynamics (DMD) and steered DMD (sDMD) simulations. We first performed binding simulations of VE-cadherin with A β species. First, we employed a EC1 cadherin dimer from the full-length of a VE-cadherin dimer to efficiently mimic the *trans* interactions (Figure 7A). From our recent study, we successfully demonstrated that the EC1 dimer was a suitable model to evaluate the dimer stability in the presence and absence of gold nanoparticles (AuNPs)⁵³. Next, three different forms of A β monomer (A β _m), oligomer (A β _o), and tetramer seed (A β _s) were prepared to assess their interactions with the cadherin dimer and how the binding disrupted the dimer (Figure 7B and **Experimental Section**). The three different forms of A β were randomly located near the EC1 dimer, and 40 independent binding

DMD simulations for 50 ns were performed. For the binding simulations, we computed the binding frequencies of the peptide species with the EC1 dimer. We observed that each form of A β entailed distinct binding behaviors with the EC1 dimer (Figure 7C). Our recent study revealed that an AuNP coated with citric acids preferred to bind the turn region of the dimer mostly consisted of cationic amino acids⁵³. Similarly, we observed that the A β_0 highly bound to the turn regions of the EC1 dimer, however, the A β_s mostly bound to the C-terminus of the dimer while the A β_m bound to the entire region of the dimer. The colored binding frequencies on the surface of the EC1 dimer detailed the binding behaviors of the A β species with the EC1 dimer (Figure 7D). Such different binding behaviors can also be verified by computing the binding frequency of the EC1 dimer with the A β species (**Figure S3A**). We figured out that the first 10 residues of A β_0 and middle 15 residues (15-30) of A β_s mostly interacted with the EC1 dimer, where all amino acids of the A β_m highly bound to the EC1 dimer. Except for the monomer, the preferred binding sites of the A β_0 and A β_s with the EC1 dimer were different from each other due to the distinct conformations of the A β nanoparticulates (**Figure S3B**).

After the binding DMD simulations, all-atom sDMD simulations were carried out to understand the EC1 dimer stability in the presence and absence of the A β species. For the sDMD simulations, one of the EC1 domains was immobilized and the other side of the domain stayed flexible. Constant forces in the range of 0-60 pN with 10 pN of windows were applied to the flexible domain of the EC1 dimer toward to the EC2 domain of the VE-cadherin dimer (Figure 7E). Subsequently, we performed 70 independent sDMD simulations with randomized initial velocities assigned according to Maxwell-Boltzmann distribution and each sDMD simulation lasted for 100 ns. Then, we evaluated the dimer stability with and without A β species by violin plots as a function of first mean dissociation time and applied forces after the sDMD simulations (Figure 7G-I). The first mean dissociation time was determined when the number of contacts at the dimer interfaces was reduced to zero. Here, we note that the 100 ns of the dissociation time means that the EC1 dimer stayed associated during the sDMD simulations. We observed that the A β_0 significantly increased the probability of early cadherin dimer dissociation, followed by the seed. Specifically, A β_0 elicited the highest cadherin dimer dissociation under the low force range (0-30 pN). However, the effect of A β_m on the dimer disruption was negligible for all applied forces. Representative trajectories of the A β_0 - and A β_s -EC1 complexes reflected the early dissociation of the cadherin dimer (**Figure 7J and K**). A β_m was detached from the dimer at an early stage or moved around during the sDMD simulations due to the flexible nature of the monomer (**Figure S4**). To confirm the reduced cadherin dimer stability, we measured the RMSF of the flexible domain of the EC1 dimer (Figure 7F). In a recent study⁵³, we showed that a reduced entropy disrupted the inherent function of a cadherin dimer. Our calculated RMSF results indicated that the A β_0 and A β_s considerably reduced the overall RMSF, while A β_m slightly reduced the RMSF for some amino acids. Although the A β species and the EC1 dimer in the simulations were not entirely the same sizes as in the experiments due to the high computational costs, the overall tendencies of the violin plots agreed well with the experimental data (Figures 3, 5, 6). Taken together, our computational results demonstrated A β -induced cadherin disruption and further revealed their corresponding dissociation mechanisms on the molecular scale.

3. Conclusion

Molecular assembly of proteins and peptides is, in essence, a remarkable nanotechnology employed by biological systems to render functional and pathogenic outcomes. Within the framework of AD, the self-assembly of A β_m into oligomers, protofibrils and amyloid fibrils entails rich pathogenic implications that are not fully understood, as reflected by a lack of success in clinical trials targeting protein amyloid aggregation. While CAA and compromised BBB usually accompany the symptoms of dementia¹⁴, the exact cause of cerebral vascular damage and their relationship with the development of AD remain unclear, with ROS production, inflammation, and the physical breakdown of tight junctions implicated as causative instigated by A β , Tau and apolipoprotein E, among others^{14,15,17,21-23}.

In this study, we discovered that the oligomers and seeds but not monomers or fibrils of anionic amyloidogenic proteins, either pathogenic (i.e., A β and α S) or functional (i.e., FapC), ubiquitously elicited APEL in HMVECs whose characteristics were reminiscent of NanoEL, a biological phenomenon entailed by inorganic nanoparticles of certain size (<100 nm) and charge (anionic or near neutral)²⁹. Specifically, our signaling pathway and transwell assays as well as fluorescence imaging, complemented with atomistic DMD and sDMD simulations, revealed disruption to the VE-cadherin machinery introduced by A β_o and A β_s . In contrast, A β_m , A β_f and all three forms of cationic IAPP were incompetent in inciting APEL. These findings suggested that, aside from size and charge to fit within the finite paracellular space and evade endocytosis, the stiffness of amyloid proteins, elevated in the oligomers and protofibrils than the monomers due to β -sheets stacking through fibrillization (**Figures S5&S6**), could also play a role in the occurrence of APEL.

Notably, our signaling pathway assays revealed that APEL was independent of ROS production, cytotoxicity and endocytosis but mediated by the protein nanoparticulates engaged with the extracellular domains of VE-cadherins, triggering intracellular actin network reorganization as well as intercellular gap formation (**Figures 3-5**). These latter findings were consistent with that of NanoEL but distinguished sharply from the existing literature linking vasculature damage and AD^{13,59}, both in terms of the mechanisms and the spatiotemporal characteristics of intercellular gap formation. In light of the bodily distributions of the vasculature and amyloid proteins, the mechanism of amyloid protein aggregates navigating through the paracellular space of the endothelium appears broadly applicable to elucidating the coexistence of AD and PD pathologies with vasculature damage^{15,17,59,60}, the selective neuronal pathology incited by systemic administration of α S⁶¹, and the curious cross-talks between the amyloidogeneses pertinent to AD, PD, prion diseases, and T2D^{12,62-64}.

4. Experimental Section/methods

A β , IAPP and α S sample preparations: 1 mg of A β (AnaSpec Inc., purity \geq 95%) and IAPP (AnaSpec Inc., purity \geq 95%) were treated with 1 mL of hexafluoro-2-propanol (HFIP, Sigma Aldrich, USA) for 3 h at room temperature to break down the pre-existing aggregates. Then the solutions were aliquoted and freeze-

dried for future use. The dried A β was dissolved in 0.1% NH₄OH and further diluted in MilliQ H₂O to a required stock concentration. The dried IAPP, lyophilized aS (AlexoTech) and FapC were respectively dissolved in MilliQ H₂O.

To acquire different species of the amyloid proteins, the aqueous solutions of A β , IAPP, aS and FapC were incubated at 37°C and allowed to fibrillate for different times according to a thioflavin T (ThT) kinetic assay. The seeds were derived from sonicated mature fibrils of different amyloid proteins using a Vibra-Cell™ Ultrasonic VCX 750 sonicator equipped with a 3 mm microtip. 2 min sonication at 20% of the maximum output power of the sonicator was applied.

Thioflavin T kinetic assay

For the ThT assay, a 50 μ L aqueous solution of 100 μ M IAPP, 100 μ M A β , 100 μ M aS or 50 μ M FapC were incubated with 200 μ M of ThT respectively in a black, clear bottom 96-well plate at 37 °C. The incubation conditions were kept the same for all the amyloid proteins except for aS, where glass beads were added into each well and shaken at 200 rpm for 5 min before reading⁶⁵. The fluorescence intensity was recorded with excitation at 440 nm and emission at 484 nm on a microplate reader (CLARIOstar, BMG LABTECH). All experiments with the samples were performed in triplicate.

Transmission electron microscopy

TEM images of all amyloid proteins at different time points according to the ThT result were acquired using a Tecnai F20 electron microscope (200 kV). 10 μ L of each sample was placed onto glow discharged formvar/carbon coated copper grids (400 mesh, Proscitech) and blotted after 1 min incubation. The sample-coated grids were negatively stained with 5 μ L of 1% uranyl acetate (UA) for 30 s. The grids were blotted and left to air dry before imaging.

Attenuated total reflection-Fourier transform infrared (ATR-FTIR) spectroscopy: FTIR spectra (1580-1700 cm⁻¹) that contained the amide I regions of each amyloid protein at different stages of fibrillization (monomeric/oligomeric/protofibrillar/fibrillar/seeds) were acquired with an IRTtracer-100 (Shimadzu) spectrometer, which was equipped with a He-Ne laser and an MCT detector (Hg-Cd-Te). The MCT detector was constantly being cooled with liquid nitrogen. Regarding sample preparation, the peptide samples were prepared as described above and incubated at 37°C at 100 μ M concentration. Concentration for the fibrillar FapC solution was 50 μ M. The collection of the oligomeric/protofibrillar or fibrillar species included a 100 μ L acquisition and further lyophilization using a freeze-drier at appropriate timepoints depending on the aggregation rates of the peptides accordingly (A β _o: 4 h, A β _{o-p}: 17 h, A β _f: 42 h, aS_o: 22 h, aS_f: 96 h, IAPP_o: 1 h, IAPP_f: 24 h). Lyophilized samples were further dissolved with 5 μ L of MilliQ H₂O and added to the top of the reservoir. Air-drying then followed using a heat gun. Samples containing monomeric species were in the powder form during spectrum acquisition. Data acquisition included the absorbance (%) measurement mode with 512 number of scans. All spectra were acquired with 4 cm⁻¹ resolution and signals were processed with the Happ-Genzel apodization function. Peak deconvolution

that generated the Gaussian band profile for each selected peak on each amide I region was performed with the built-in PeakDeconvolution application through Origin Software (Origin Lab). Deconvoluted band regions were assigned to each type of secondary structure following previous reports⁶⁶.

Cell culture

Human dermal microvascular endothelial cells (HMVECs) were obtained from Lonza (Switzerland) and cultured in complete EndoGRO-MV-VEGF growth medium (Merck Millipore, USA). hCMEC/D3 human brain endothelial cells were derived from Merck Millipore (USA) and cultured in complete endothelial cell medium (ScienCell, USA). All cell culture was performed under a standard culture condition (37°C, 5% CO₂). In all experiments, endothelial cells were seeded at an initial density of 40,000 cells/cm² and were cultured to form a confluent monolayer before subsequent treatments.

Cell viability assay

HMVECs were seeded into 96-well plates and cultured overnight, before being incubated with the amyloid proteins at 20 µM, for durations of 0 h, 0.5 h, 1 h or 2 h. Each group consisted of three biologically independent samples. The cells were subsequently washed with 1× PBS (phosphate-buffered saline). alamarBlue reagent (Life Technology, USA), prepared in cell media at the recommended concentration by the manufacturer, was added to cells and incubated for 2 h. Fluorescence readings were collected on a microplate reader (Hidex, Finland), at wavelengths of 560/590 nm (excitation/emission). Measurements from all treatment groups were normalized against the measurements from negative (untreated) control group. H₂O₂ (200 µM) served as positive control.

ROS production assay

HMVECs were cultured in 96-well plates and treated with 20 µM of various amyloid proteins for the durations of 0 h, 0.5 h, 1 h or 2 h. Each treatment group was made up of three independent replicates. After washing with PBS, cells were incubated for 30 min with a mixture of the ROS detector 2',7'-dichlorodihydrofluorescein diacetate (H₂DCFDA, 1 µM; Merck, USA) and Hoechst 33342 (1 µg/mL; Sigma Aldrich, USA). Fluorescence measurements were taken on a microplate reader, at excitation/emission of 495/527 nm (H₂DCFDA) and 350/461 nm (Hoechst 33342). H₂DCFDA readings were normalized against respective Hoechst readings to account for cell numbers. Readings from the untreated control group were further used to normalize the other groups' readings. Positive control was H₂O₂ (200 µM).

Immunofluorescence staining of in vitro samples: HMVECs were grown on 8-well chamber slides to reach confluent monolayers. After being treated with different amyloid proteins for 30 min, cells were gently washed with Hank's balanced salt solution (HBSS) and fixed by 4% paraformaldehyde for 15 min, followed by permeabilizing and blocking with 0.1% saponin and 5% horse serum in PBS/azide for 1 hour at room temperature. Thereafter, fixed cells were washed three times with PBS and incubated overnight at 4°C with primary rabbit anti-VE-cadherin antibody (Abcam) at 1:400 dilution with 5% horse serum in PBS/azide. Then the cells were washed with PBS and incubated with secondary donkey anti-rabbit Alexa

Fluor 594 antibody (1:500, Abcam) and Phalloidin-iFluor 488 (1:1000, Abcam) in PBS/azide solution for 2 h at room temperature. After nuclei staining with Hoechst 33342 (Sigma Aldrich, USA) at 1:2000 dilution for 5 min, the cells were imaged with Leica SP8 lightening confocal microscope (Leica, Germany) and semiquantitative analysis was performed using ImageJ.

Treatments prior to exposure to A β samples

In assays that involve pre-treatments, the cultured HMVECs were exposed to the respective treatments, which were supplemented into complete EndoGRO-MV-VEGF growth medium, for a duration of 1 h. For experiments with antioxidants, the pre-treatment involved N-acetyl cysteine (NAC, 10 μ M; Sigma Aldrich, USA), which was used to alleviate ROS production. For experiments about endocytosis, the inhibitors monodansyl cadaverine (MDC, 10 μ M; Sigma Aldrich, USA) and methyl β -cyclodextrin (M β CD, 5 mM; Sigma Aldrich, USA) were used as a cocktail to inhibit endocytosis. For experiments related to cell signaling, the Rho-associated protein kinase inhibitor Y-27632 (Sigma Aldrich, USA) and Src family tyrosine kinase inhibitor PP1 (Sigma Aldrich, USA) were employed at 10 μ M in complete growth medium. After the pre-treatment, the medium was replaced with fresh growth medium now containing respective A β species and the same antioxidant/inhibitor(s). Growth medium treatment that contained the antioxidant/inhibitor(s) but no A β species acted as negative control. The usage of BV-6 antibody as a pre-treatment was described under “competitive inhibition assay” instead.

Transwell insert assays

In general, HMVECs were cultured on transwell inserts (polycarbonate membrane, 0.4 μ m pore diameter; Corning Costar, USA) in a 24-well plate until the formation of a confluent layer (seeded at density of 40,000 cells/cm 2 , 2 days). HMVECs were treated with different types and concentrations of the amyloid proteins that were supplemented into complete EndoGRO-MV-VEGF growth medium, for the stated durations. Subsequently, A β treatments were removed and the wells were washed with PBS. Fresh media with FITC-dextran (1 mg/mL, 40 kDa; Sigma Aldrich, USA) were then added to quantitatively determine permeability in endothelial barriers. After 30 min exposure to FITC-dextran treatment, solutions in the lower compartment were sampled (100 μ L) and their fluorescence was recorded by a microplate reader (Hidex, Finland) at wavelengths of 490/520 nm (excitation/emission). The degree of FITC-dextran transport was defined as fluorescence reading from a treated group normalized by its corresponding untreated control.

Competitive inhibition assay: Confluent HMVECs cultured on 8 well chamber slides were incubated with VE-cadherin BV-6 antibody (1:100; Millipore) in medium containing 3% fetal bovine serum for 1 h. VE-cadherin BV-6 antibody specifically recognizes the extracellular domain of VE-cadherin. Cells were washed with HBSS and subsequently incubated with A β s for 30 min. Then, immunofluorescence staining was performed to observe the leakiness.

Association of A β s and VE-cadherin assay

Confluent HMVECs were incubated with ThT-labeled A β _s for 30 min, which were derived from the fibrils in the ThT assay. After that, excess A β _s were removed, and the cells were washed with HBSS.

Immunofluorescence staining was performed to observe the location of ThT-labeled A β _s and VE-cadherin.

Immunoblotting: HMVECs were cultured in 6 cm cell culture dishes and subjected to the pre-treatment of PP1 inhibitor in fresh cell medium or fresh medium only. Subsequently, HMVECs were exposed to different concentrations of A β ₀ and A β _s for 1 h. Following the exposure, each dish was washed thrice with chilled PBS and lysed with Laemmli sample buffer (63 mM Tris-HCl pH 6.8, 2% sodium dodecyl sulphate (SDS), 10% glycerol, 1% 2-mercaptoethanol and 0.0005% bromophenol blue). The cell lysis buffer solution had been supplemented with a cocktail of 1% protease and phosphatase inhibitors (Sigma Aldrich, USA). Gel electrophoresis was conducted with the derived cell lysates using 10% resolving polyacrylamide gels (Mini Protean, Bio-Rad, USA) and proteins transferred onto nitrocellulose membranes (Sigma Aldrich, USA). The membranes were blocked with 5% bovine serum albumin (BSA) solution for 1 h and incubated with a solution of the relevant primary antibody overnight at 4°C. Subsequently, membranes were washed thrice and then incubated in a solution of relevant horseradish peroxidase (HRP)-conjugated secondary antibody for 1 h. Membranes were exposed to Immobilon Western Chemiluminescent HRP substrate kit (Merck, USA) and protein bands were captured visually through a chemiluminescence imaging system (Syngene, UK). Expression levels of proteins in images were analyzed semi-quantitatively through ImageJ software and normalized against respective control group's protein band within each image. In all washing steps, as well as preparation of blocking and antibody solutions, Tween 20 detergent (TBST; composed of: 150 mM NaCl, 20 mM Tris-HCl, 0.1% Tween 20) was used. Primary antibodies were used at dilution of 1:1000 and secondary HRP-conjugated antibodies were employed at 1:2500. The complete list of antibodies utilized for immunoblotting are provided in **Table S2**.

Ex vivo vascular leakiness assay

For the *ex vivo* vascular leakiness assay, swine vessels were obtained from a local slaughterhouse in Chongqing. Three pigs were used, the blood vessels of each pig were taken out and used for one experiment in 3 groups, and the experiment was repeated 3 times for three pigs. Briefly, blood vessels of the coronary artery were cut transversely into individual pieces and placed in a commercial transwell chamber after removal of its original membranes. The blood vessel areas we took could surround the entire internal space of the transwell inserts. A β species of 200 μ M and 400 μ M were added to the custom-made swine vessel transwell device and incubated for 6 h. After the exposure, the A β -containing solution was discarded and then Evans blue dye (EBD, 100 mM) was added to each well for an additional 1 h. During the experiment, transwell inserts were placed in a 24-well plate, and then the 24-well plate was placed at 37°C for static culture. Finally, the fluorescence from the lower compartment of the transwell was acquired at 624 nm with a microplate reader. Readout from the negative control group was used for normalization.

In vivo leakiness assay of A β _s and A β ₀: All *in vivo* mice experiments were approved by the Southwest University Animal Care and Use Committee. Experiments were carried out according to the NIH's

guidelines for the care and use of laboratory animals. Adult, 10 weeks old, male Swiss mice were obtained from Ensiweiier Biotechnology Co, Ltd. (Chongqing, China). Mice were supplied with free access of food and water and were kept at standard temperature in a humid environment with a light/dark cycle of 12 h. Mice received once intravenous injection 100 µg A_β_s-containing 10 mM Evans blue dye solution or 100 µg A_β_o-containing 10 mM Evans blue dye solution. The control mice received once intravenous injection of 10 mM EBD solution. After 24 h, the mice were sacrificed to obtain the brains for imaging by using NEWTON 7.0 Imaging System.

Immunofluorescence staining of mice brain samples: Mice experiments were approved by the Southwest University Animal Care and Use Committee. Adult, 10 weeks old, male Swiss mice were supplied with free access of food and water were kept at standard temperature in a humid environment with a light/dark cycle of 12 h. Mice received one intravenous injection 100 µg A_β_s-containing 10 mM EBD solution or 100 µg A_β_o-containing 10 mM EBD solution. The control mice received once intravenous injection of 10 mM EBD solution. After 24 h, the mice were sacrificed to obtain the brains. The brains were fixed in 4% paraformaldehyde solution and removed after 48 h. They were then embedded with optimal cutting temperature (OCT) compound and sliced in a transverse section by a freezing microtome. Then, slices were incubated with 10% skimmed milk for 2 h, then incubated with anti-A11 antibody (1:250 dilution) for 3 h. Alexa Fluor 488-conjugated secondary antibody (1:250 dilution) was used for fluorescence detection. DAPI was used for the visualization of nuclei and then imaged with a super-resolution laser confocal microscope (Nikon, N-SIME).

DMD simulations for amyloid and EC1 cadherin dimer binding: All-atom discrete molecular dynamics (DMD) simulation with implicit solvent models was used for this study to characterize the A_β induced VE-cadherin dissociation. DMD is a unique category of molecular dynamics (MD) with significantly enhanced sampling efficiency, which has been widely applied to biomolecular studies such as protein folding, peptide aggregation^{67–69}, and understanding the protein structure and dynamics^{70,71}. The details of the DMD algorithm were described in our previous studies^{67–69}. From our recent study, it has been demonstrated that the EC1 dimer from full-length VE-cadherin was suitable model to characterize the *trans* interaction mimicking the cadherin dimer coming from two opposing cells. Therefore, the EC1 cadherin dimer adapted from the cryo-EM model of EC12 cadherin dimer was considered (PDB ID: 3PPE⁷²) for the current study. For constructing the molecular model of EC1 dimer for this study, the bond constraints for calcium ion sites (i.e., residues Glu11, Asp62, Glu64, Asp96, and Asp99) and Gō-potential were applied to the domain-swapped region of the EC1 dimer, respectively (Figure 7A). Specifically, the weak contact energy of 0.4 kcal/mol (~0.67 K_BT) was assigned to C_β atoms of contacting residues. Next, we prepared three different forms of A_β₄₂ monomer (A_β_m), oligomer (A_β_o), and tetramer seed (A_β_s). The atomic models of A_β_m (PDB ID: 1IYT⁷³) and A_β_s (PDB ID: 5OQV⁷⁴) were used, and A_β_o was brought from our recent work⁷⁵. To consider the A_β_s model, the seed was relaxed and equilibrated for 50 ns with the application of Gō-constraints between each peptide. Same contact energy of Gō-potential applied on EC1 dimer was assigned to the inter-peptides of A_β_s. Each amyloid peptide was randomly located away from

the EC1 dimer at least 12 Å away in a 150 nm³ cubic box and counter ions were distributed to neutralize the net charge. To avoid a biased potential energy, different initial velocity was applied and 40 independent DMD simulations each of 50 ns (an accumulative 2.0 μs DMD simulations) were performed. 50 fs/step of the unit simulation time and 1 kcal/mol of corresponding energy were employed and a temperature of 300 K was maintained with Anderson's thermostat. After the binding simulations, we computed the binding frequencies of the amyloid proteins with the EC1 dimer from the last 20 ns of binding simulations. To calculate the binding frequency, we assigned 0.65 nm of cutoff distance to get an atomistic contact between the EC1 cadherin dimer and amyloid proteins.

Steered discrete molecular dynamics (sDMD) simulations

We employed sDMD simulations to identify the effects of amyloid proteins on VE-cadherin dimer disruption. This constant force-pulling *in silico* experiments generally mimic the experimental force spectroscopy methods such as atomic force microscopy (AFM) and optical tweezers. With respect to applying either a constant force or a velocity, this technique enables to characterize protein unfolding, protein structure and dynamics. To carry out the sDMD simulation, we immobilized one of the EC1 domains and made flexible of the other domain⁵³. Constant forces were applied to the flexible domain of the EC1 cadherin dimer towards to the EC2 cadherin dimer (Figure 7E). 10 pN of interval forces in the range of 0~60 pN was given during the sDMD simulations. For sufficient sampling, 70 cases of independent sDMD simulations each for 100 ns were performed. The detailed conditions for running the sDMD simulations were the same as for the binding simulation of the cadherin dimer and amyloid proteins.

Declarations

Acknowledgements

This work was supported by the National Key Research and Development Program, Ministry of Science and Technology of China (2021YFA1200903), National Natural Science Foundation of China (21976145, 21974110 and 82104087), National Science Foundation (CAREER CBET-1553945) and National Institutes of Health (MIRA R35GM119691). The authors wish to thank Scott Peng and Kairi Koppel for their technical assistance.

Conflict of Interest

The authors declare no conflict of interest.

Author contributions

PCK and DTL conceived the project. PCK, DTL, FD and YS designed the project. YL, NN, WW, ML and PCK wrote the manuscript. YL, NA and AK performed TEM, FTIR, confocal fluorescence microscopy, *in vitro* transwell, as well as gap area analysis. NN performed *in vitro* transwell, signaling pathway, viability, ROS

and endocytosis assays. WW performed *ex vivo* and *in vivo* assays. ML performed DMD and sDMD simulations. All authors discussed and agreed on the presentation of the manuscript.

References

1. Hardy, J. A. & Higgins, G. A. Alzheimer's Disease: The Amyloid Cascade Hypothesis. *Science* **256**, 184–185 (1992).
2. Ke, P. C. *et al.* Implications of peptide assemblies in amyloid diseases. *Chem. Soc. Rev.* **46**, 6492–6531 (2017).
3. Soto, C. *et al.* β -sheet breaker peptides inhibit fibrillogenesis in a rat brain model of amyloidosis: Implications for Alzheimer's therapy. *Nat. Med.* **4**, 822–826 (1998).
4. McLaurin, J. *et al.* Therapeutically effective antibodies against amyloid-beta peptide target amyloid-beta residues 4-10 and inhibit cytotoxicity and fibrillogenesis. *Nat. Med.* **8**, 1263–1269 (2002).
5. Bieschke, J. *et al.* Small-molecule conversion of toxic oligomers to nontoxic β -sheet-rich amyloid fibrils. *Nat. Chem. Biol.* **8**, 93–101 (2012).
6. Chen, J., Armstrong, A. H., Koehler, A. N. & Hecht, M. H. Small Molecule Microarrays Enable the Discovery of Compounds that Bind the Alzheimer's A β Peptide. *J. Am. Chem. Soc.* **132**, 17015–17022 (2010).
7. Bieschke, J. *et al.* EGCG remodels mature α -synuclein and amyloid- β fibrils and reduces cellular toxicity. *Proc. Natl. Acad. Sci. U.S.A.* **107**, 7710–7715 (2010).
8. Chen, Q. *et al.* Tau-Targeted Multifunctional Nanocomposite for Combinational Therapy of Alzheimer's Disease. *ACS Nano* **12**, 1321–1338 (2018).
9. Luo, Q. *et al.* A self-destructive nanosweeper that captures and clears amyloid β -peptides. *Nat. Commun.* **9**, 1802 (2018).
10. Zhao, Y. *et al.* Nanocomposites Inhibit the Formation, Mitigate the Neurotoxicity, and Facilitate the Removal of β -Amyloid Aggregates in Alzheimer's Disease Mice. *Nano Lett.* **19**, 674–683 (2019).
11. Javed, I. *et al.* Inhibition of amyloid beta toxicity in zebrafish with a chaperone-gold nanoparticle dual strategy. *Nat. Commun.* **10**, 3780 (2019).
12. Ke, P. C. *et al.* Half a century of amyloids: past, present and future. *Chem. Soc. Rev.* **49**, 5473–5509 (2020).
13. Long, J. M. & Holtzman, D. M. Alzheimer Disease: An Update on Pathobiology and Treatment Strategies. *Cell* **179**, 312–339 (2019).
14. Selkoe, D. J. The molecular pathology of Alzheimer's disease. *Neuron* **6**, 487–498 (1991).
15. Zipser, B. D. *et al.* Microvascular injury and blood-brain barrier leakage in Alzheimer's disease. *Neurobiol. Aging* **28**, 977–986 (2007).
16. Qosa, H., LeVine, H., Keller, J. N. & Kaddoumi, A. Mixed oligomers and monomeric Amyloid- β disrupts endothelial cells integrity and reduces monomeric amyloid- β transport across hCMEC/D3 cell line as an in vitro blood-brain barrier model. *Biochim. Biophys. Acta* **1842**, 1806–1815 (2014).

17. Nagababu, E., Usatyuk, P. V., Enika, D., Natarajan, V. & Rifkind, J. M. Vascular Endothelial Barrier Dysfunction Mediated by Amyloid- β Proteins. *J. Alzheimers Dis.* **17**, 845–854 (2009).
18. Haass, C., Kaether, C., Thinakaran, G. & Sisodia, S. Trafficking and Proteolytic Processing of APP. *Cold Spring Harb. Perspect. Med.* **2**, a006270 (2012).
19. Risacher, S. L. *et al.* Plasma amyloid beta levels are associated with cerebral amyloid and tau deposition. *Alzheimers Dement.* **11**, 510–519 (2019).
20. Bateman, R. J., Wen, G., Morris, J. C. & Holtzman, D. M. Fluctuations of CSF amyloid-beta levels: implications for a diagnostic and therapeutic biomarker. *Neurology* **68**, 666–669 (2007).
21. Thomas, T., Thomas, G., McLendon, C., Sutton, T. & Mullan, M. β -Amyloid-mediated vasoactivity and vascular endothelial damage. *Nature* **380**, 168–171 (1996).
22. Keaney, J. *et al.* Autoregulated paracellular clearance of amyloid- β across the blood-brain barrier. *Sci. Adv.* **1**, e1500472 (2015).
23. Nortley, R. *et al.* Amyloid β oligomers constrict human capillaries in Alzheimer's disease via signaling to pericytes. *Science* **365**, eaav9518 (2019).
24. Han, X.-J. *et al.* Amyloid β -42 induces neuronal apoptosis by targeting mitochondria. *Mol. Med. Rep.* **16**, 4521–4528 (2017).
25. Carrano, A. *et al.* Amyloid Beta induces oxidative stress-mediated blood-brain barrier changes in capillary amyloid angiopathy. *Antioxid. Redox Signal.* **15**, 1167–1178 (2011).
26. Wan, W. *et al.* A β 1–42 oligomer-induced leakage in an in vitro blood–brain barrier model is associated with up-regulation of RAGE and metalloproteinases, and down-regulation of tight junction scaffold proteins. *J. Neurochem.* **134**, 382–393 (2015).
27. Setyawati, M. I. *et al.* Titanium dioxide nanomaterials cause endothelial cell leakiness by disrupting the homophilic interaction of VE-cadherin. *Nat. Commun.* **4**, 1673 (2013).
28. Peng, F. *et al.* Nanoparticles promote in vivo breast cancer cell intravasation and extravasation by inducing endothelial leakiness. *Nat. Nanotechnol.* **14**, 279–286 (2019).
29. Tee, J. K. *et al.* Nanoparticles' interactions with vasculature in diseases. *Chem. Soc. Rev.* **48**, 5381–5407 (2019).
30. Tay, C. Y., Setyawati, M. I. & Leong, D. T. Nanoparticle Density: A Critical Biophysical Regulator of Endothelial Permeability. *ACS Nano* **11**, 2764–2772 (2017).
31. Setyawati, M. I., Tay, C. Y., Bay, B. H. & Leong, D. T. Gold Nanoparticles Induced Endothelial Leakiness Depends on Particle Size and Endothelial Cell Origin. *ACS Nano* **11**, 5020–5030 (2017).
32. Setyawati, M. I., Mochalin, V. N. & Leong, D. T. Tuning Endothelial Permeability with Functionalized Nanodiamonds. *ACS Nano* **10**, 1170–1181 (2016).
33. Antzutkin, O. N. Amyloidosis of Alzheimer's Abeta peptides: solid-state nuclear magnetic resonance, electron paramagnetic resonance, transmission electron microscopy, scanning transmission electron microscopy and atomic force microscopy studies. *Magn. Reson. Chem.* **42**, 231–246 (2004).

34. Mor, D. E., Ugras, S. E., Daniels, M. J. & Ischiropoulos, H. Dynamic structural flexibility of α -synuclein. *Neurobiol. Dis.* **88**, 66–74 (2016).
35. Bernstein, S. L. *et al.* α -Synuclein: Stable compact and extended monomeric structures and pH dependence of dimer formation. *J. Am. Soc. Mass Spectrom.* **15**, 1435–1443 (2004).
36. Binolfi, A., Quintanar, L., Bertoncini, C. W., Griesinger, C. & Fernández, C. O. Bioinorganic chemistry of copper coordination to alpha-synuclein: Relevance to Parkinson's disease. *Coord. Chem. Rev.* **256**, 2188–2201 (2012).
37. Azzam, S. K. *et al.* Inhibition of Human Amylin Aggregation and Cellular Toxicity by Lipoic Acid and Ascorbic Acid. *Mol. Pharmaceutics* **15**, 2098–2106 (2018).
38. Akter, R. *et al.* Islet Amyloid Polypeptide: Structure, Function, and Pathophysiology. *J. Diabetes Res.* **2016**, 2798269 (2016).
39. Christensen, L. F. B., Schafer, N., Wolf-Perez, A., Madsen, D. J. & Otzen, D. E. Bacterial Amyloids: Biogenesis and Biomaterials. in *Biological and Bio-inspired Nanomaterials: Properties and Assembly Mechanisms* (eds. Perrett, S., Buell, A. K. & Knowles, T. P. J.) 113–159 (Springer, 2019). doi:10.1007/978-981-13-9791-2_4.
40. Marco, S. & Skaper, S. D. Amyloid β -peptide1–42 alters tight junction protein distribution and expression in brain microvessel endothelial cells. *Neurosci. Lett.* **401**, 219–224 (2006).
41. Kook, S.-Y. *et al.* A β 1–42-RAGE Interaction Disrupts Tight Junctions of the Blood–Brain Barrier Via Ca $^{2+}$ -Calcineurin Signaling. *J. Neurosci.* **32**, 8845–8854 (2012).
42. Chao, A.-C., Lee, T.-C., Juo, S.-H. H. & Yang, D.-I. Hyperglycemia Increases the Production of Amyloid Beta-Peptide Leading to Decreased Endothelial Tight Junction. *CNS Neurosci. Ther.* **22**, 291–297 (2016).
43. Forrester, S. J., Kikuchi, D. S., Hernandes, M. S., Xu, Q. & Griendling, K. K. Reactive Oxygen Species in Metabolic and Inflammatory Signaling. *Circ. Res.* **122**, 877–902 (2018).
44. Butterfield, D. A. Amyloid beta-peptide (1-42)-induced oxidative stress and neurotoxicity: implications for neurodegeneration in Alzheimer's disease brain. A review. *Free Radic. Res.* **36**, 1307–1313 (2002).
45. Tsoy, A., Umbayev, B., Shalakhmetova, T. & Askarova, S. Role of ROS in A β 42 Mediated Activation of Cerebral Endothelial Cells. *Cent. Asian J. Glob. Health* **3**, 179 (2014).
46. Yatin, S. M., Varadarajan, S. & Butterfield, D. A. Vitamin E Prevents Alzheimer's Amyloid beta-Peptide (1-42)-Induced Neuronal Protein Oxidation and Reactive Oxygen Species Production. *J. Alzheimers Dis.* **2**, 123–131 (2000).
47. Bortner, C. D. & Cidlowski, J. A. Apoptotic volume decrease and the incredible shrinking cell. *Nature* **9**, 1307–1310 (2002).
48. Takada, E. *et al.* Molecular Mechanism of Apoptosis by Amyloid β -Protein Fibrils Formed on Neuronal Cells. *ACS Chem. Neurosci.* **11**, 796–805 (2020).
49. Itoh, N. *et al.* Not Oligomers but Amyloids are Cytotoxic in the Membrane-Mediated Amyloidogenesis of Amyloid- β Peptides. *ChemBioChem* **19**, 430–433 (2018).

50. Fossati, S., Ghiso, J. & Rostagno, A. Insights into Caspase-Mediated Apoptotic Pathways Induced by Amyloid- β in Cerebral Microvascular Endothelial Cells. *Neurodegener Dis.* **10**, 324–328 (2012).
51. Elmore, S. Apoptosis: A Review of Programmed Cell Death. *Toxicol. Pathol.* **35**, 495–516 (2007).
52. Chaitanya, G. V., Alexander, J. S. & Babu, P. P. PARP-1 cleavage fragments: signatures of cell-death proteases in neurodegeneration. *Cell Commun. Signal.* **8**, 31 (2010).
53. Lee, M. *et al.* A Framework of Paracellular Transport via Nanoparticles-Induced Endothelial Leakiness. *Adv. Sci.* **8**, 2102519 (2021).
54. Adam, A. P., Sharenko, A. L., Pumiglia, K. & Vincent, P. A. Src-induced Tyrosine Phosphorylation of VE-cadherin Is Not Sufficient to Decrease Barrier Function of Endothelial Monolayers. *J. Biol. Chem.* **285**, 7045–7055 (2010).
55. Schnittler, H. *et al.* Actin filament dynamics and endothelial cell junctions: the Ying and Yang between stabilization and motion. *Cell Tissue Res.* **355**, 529–543 (2014).
56. Bazzoni, G. & Dejana, E. Endothelial Cell-to-Cell Junctions: Molecular Organization and Role in Vascular Homeostasis. *Physiol. Rev.* **84**, 869–901 (2004).
57. Vestweber, D., Broermann, A. & Schulte, D. Control of endothelial barrier function by regulating vascular endothelial-cadherin. *Curr. Opin. Hematol.* **17**, 230–236 (2010).
58. Liao, J. K., Seto, M. & Noma, K. Rho Kinase (ROCK) Inhibitors. *J. Cardiovasc. Pharmacol.* **50**, 17–24 (2007).
59. Klohs, J. An Integrated View on Vascular Dysfunction in Alzheimer's Disease. *Neurodegener Dis.* **19**, 109–127 (2019).
60. Smith, E. E. & Greenberg, S. M. β -Amyloid, Blood Vessels, and Brain Function. *Stroke* **40**, 2601–2606 (2009).
61. Kuan, W.-L. *et al.* Systemic α -synuclein injection triggers selective neuronal pathology as seen in patients with Parkinson's disease. *Mol. Psychiatry* **26**, 556–567 (2021).
62. Masliah, E. *et al.* β -Amyloid peptides enhance α -synuclein accumulation and neuronal deficits in a transgenic mouse model linking Alzheimer's disease and Parkinson's disease. *Proc. Natl. Acad. Sci. U.S.A.* **98**, 12245–12250 (2001).
63. Morales, R. *et al.* Molecular Cross Talk between Misfolded Proteins in Animal Models of Alzheimer's and Prion Diseases. *J. Neurosci.* **30**, 4528–4535 (2010).
64. Guo, J. L. *et al.* Distinct α -Synuclein Strains Differentially Promote Tau Inclusions in Neurons. *Cell* **154**, 10.1016/j.cell.2013.05.057 (2013).
65. Andrikopoulos, N. *et al.* Inhibition of Amyloid Aggregation and Toxicity with Janus Iron Oxide Nanoparticles. *Chem. Mater.* **33**, 6484–6500 (2021).
66. Jackson, M. & Mantsch, H. H. The Use and Misuse of FTIR Spectroscopy in the Determination of Protein Structure. *Crit. Rev. Biochem. Mol. Biol.* **30**, 95–120 (1995).
67. Sun, Y., Wang, B., Ge, X. & Ding, F. Distinct Oligomerization and Fibrillization Dynamics of Amyloid Core Sequences of Amyloid-beta and Islet Amyloid Polypeptide. *Phys. Chem. Chem. Phys.* **19**,

28414–28423 (2017).

68. Sun, Y., Ge, X., Xing, Y., Wang, B. & Ding, F. β -barrel Oligomers as Common Intermediates of Peptides Self-Assembling into Cross- β Aggregates. *Sci. Rep.* **8**, 10353 (2018).
69. Sun, Y. *et al.* Amyloid self-assembly of hIAPP8-20 via the accumulation of helical oligomers, α -helix to β -sheet transition, and formation of β -barrel intermediates. *Small* **15**, e1805166 (2019).
70. Yanez Orozco, I. S. *et al.* Identifying weak interdomain interactions that stabilize the supertertiary structure of the N-terminal tandem PDZ domains of PSD-95. *Nat. Commun.* **9**, 3724 (2018).
71. Basak, S. *et al.* Probing Interdomain Linkers and Protein Supertertiary Structure In Vitro and in Live Cells with Fluorescent Protein Resonance Energy Transfer. *J. Mol. Biol.* **433**, 166793 (2021).
72. Brasch, J. *et al.* Structure and binding mechanism of vascular endothelial cadherin, a divergent classical cadherin. *J. Mol. Biol.* **408**, 57–73 (2011).
73. Crescenzi, O. *et al.* Solution structure of the Alzheimer amyloid β -peptide (1–42) in an apolar microenvironment. *Eur. J. Biochem.* **269**, 5642–5648 (2002).
74. Gremer, L. *et al.* Fibril structure of amyloid- β (1-42) by cryo-electron microscopy. *Science* **358**, 116–119 (2017).
75. Sun, Y. *et al.* Spontaneous formation of β -sheet nano-barrels during the early aggregation of Alzheimer's amyloid beta. *Nano Today* **38**, 101125 (2021).

Figures

A	hIAPP KONTATACATORLANFLVHSSNNFGAILSSTNVGSNTY	37
	Aβ₁₋₄₂ DAEFRHDSGYEVHHQKLVFFAEDVGSNKGAIIIGLMVGGVIA	42
	α-synuclein MDVFMKGLSKAEGVVAEEAKTKQGVAEAAGKTKEGVLYVGSKTKEGVVHGVAATVAEKTKEQVTNVGGAVVTGVTAVAQKTVEGAGSIAAAATGFVKKDQL GKNEEGAPQEGLIEDMPVDPDNEAYEMPSEEQYQDYEPKA	100 140
	FapC MKPTMALKPLVFALAAALMAVAAQAGPAEKWKPTPAPTGTVAAGVTDTQVSKDNNFKDDTCKTLNNAGANGSLNSNSKGNLGANIAAGSGNQQDNAAAATSSAG DAATVFAVADIVQESKDKNFTNKGCTQNALLNSANNSCNVGVNVAAGQGNQQKNNLAIVTADGKNAASNTEQVSLDNHFLNEASSKHSHYKPQYVVN NAGLLNSANNASGNIGVNVAAGAGNQGSNTLTLGGCTVCAAGTGSKLAF	100 200 250

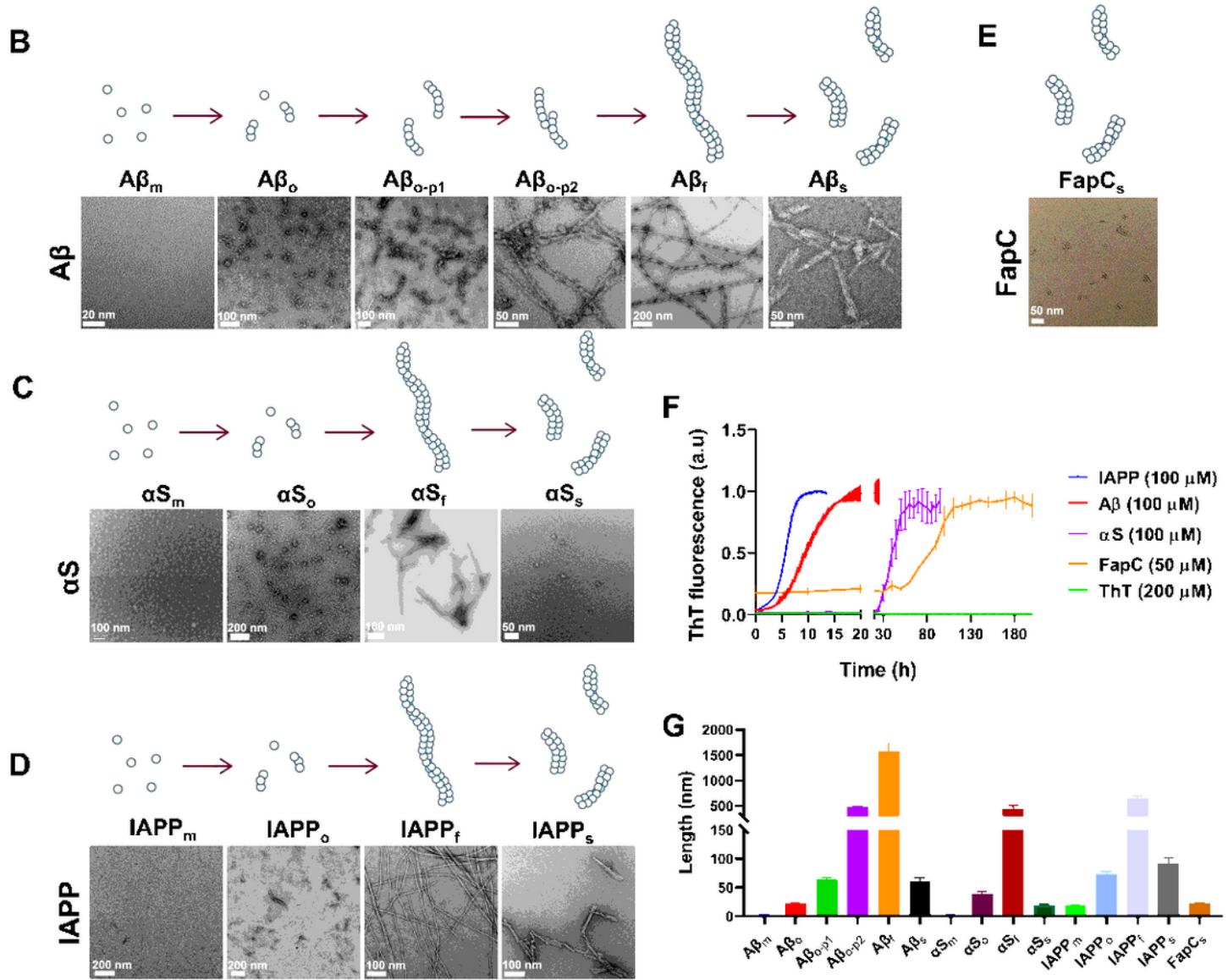


Figure 1

Characterizations of different aggregates of pathogenic (A β , α S, IAPP) and functional (FapC) amyloid proteins. (A) Amino acid sequences of the four amyloid proteins used in the study. Red: negative charge, green: hydrophobic, blue: positive charge, orange: polar uncharged amino acids, and gray: special cases. (B-E) Transmission electron microscopy imaging of different amyloid protein species: (B) A β , (C) α S, (D) IAPP and (E) FapC. The label "m" stands for monomers, "o" for oligomers, "o-p1" and "o-p2" refer to

phases of protofibrils, "f" for fibrils, and "s" for sonicated seeds, respectively. (F) ThT kinetic assay of amyloid protein fibrilization. (G) Lengths of different amyloid protein aggregates based on TEM imaging.

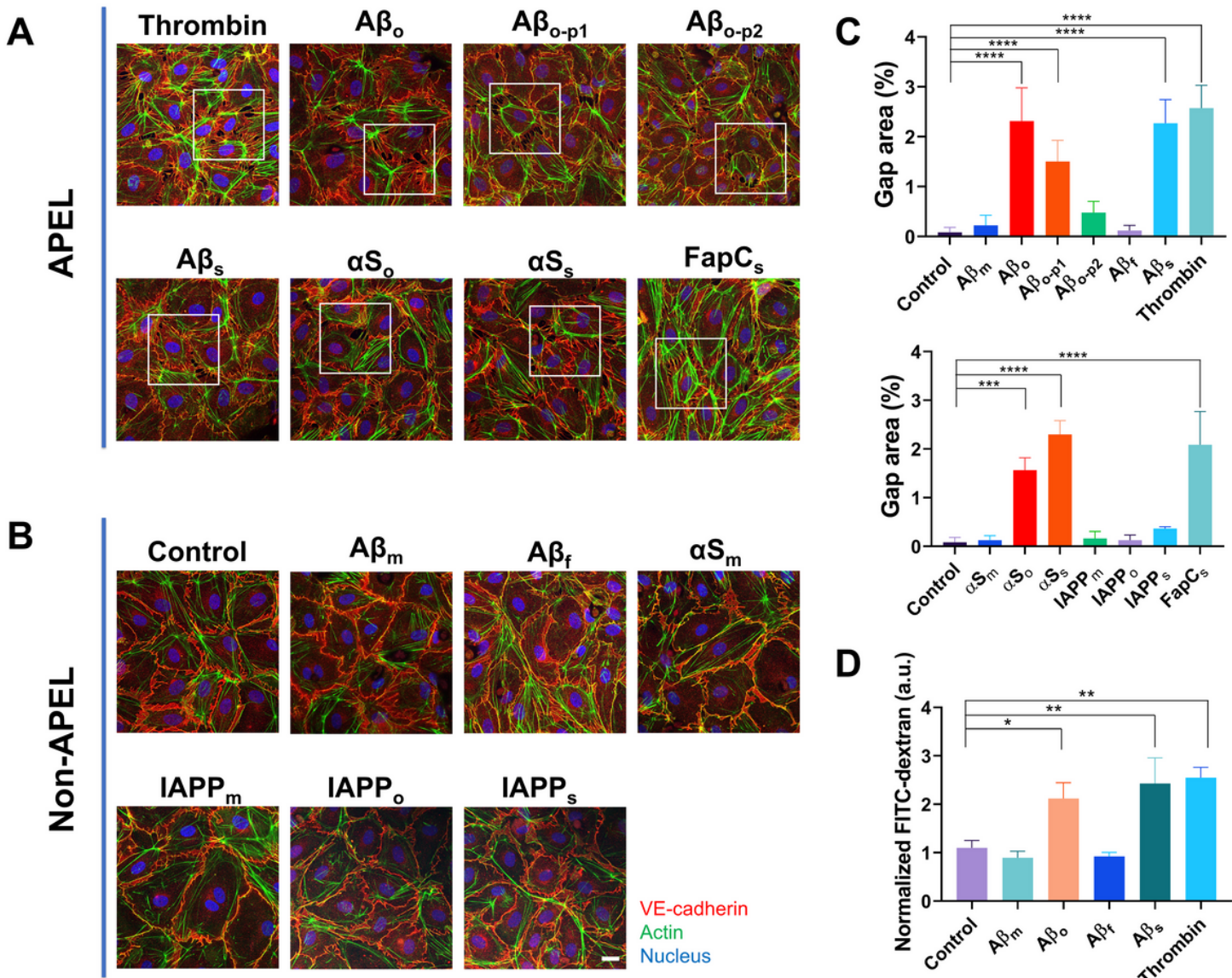


Figure 2

Induced endothelial leakiness observed in HMVECs treated with anionic A β , α S and FapC aggregates, but no samples of cationic IAPP induced significant leakiness. (A, B) Confocal fluorescence microscopy revealed endothelial leakiness with different peptide species (all 20 μM), including A β oligomers ($\text{A}\beta_o$), protofibrils ($\text{A}\beta_{o-p1}$, $\text{A}\beta_{o-p2}$) and seeds ($\text{A}\beta_s$), α S oligomers (αS_o) and seeds (αS_s), and FapC seeds (FapC_s), upon 30 min treatments. The monomers $\text{A}\beta_m$ and αS_m , as well as fibrils $\text{A}\beta_f$, could not induce endothelial leakiness in HMVECs. No endothelial leakiness was observed in the presence of all three forms of IAPP. Scale bar = 20 μm . Red: VE-cadherin, green: actin, blue: nuclei. Scale bar = 20 μm . (C) Gap area percentages were analyzed via ImageJ according to the images related to panels A and B. (D) Transwell

assay quantitatively revealed occurrence of endothelial leakiness after 30 min incubation with the different forms of A β . Thrombin (3 U/mL) acted as positive control of induced leakiness. Data are shown as mean \pm SD (n=3), analyzed via one-way ANOVA using GraphPad Prism 8, *represents P < 0.05, ** represents P < 0.01, *** represents P < 0.001 and **** represents P < 0.0001 between the compared groups.

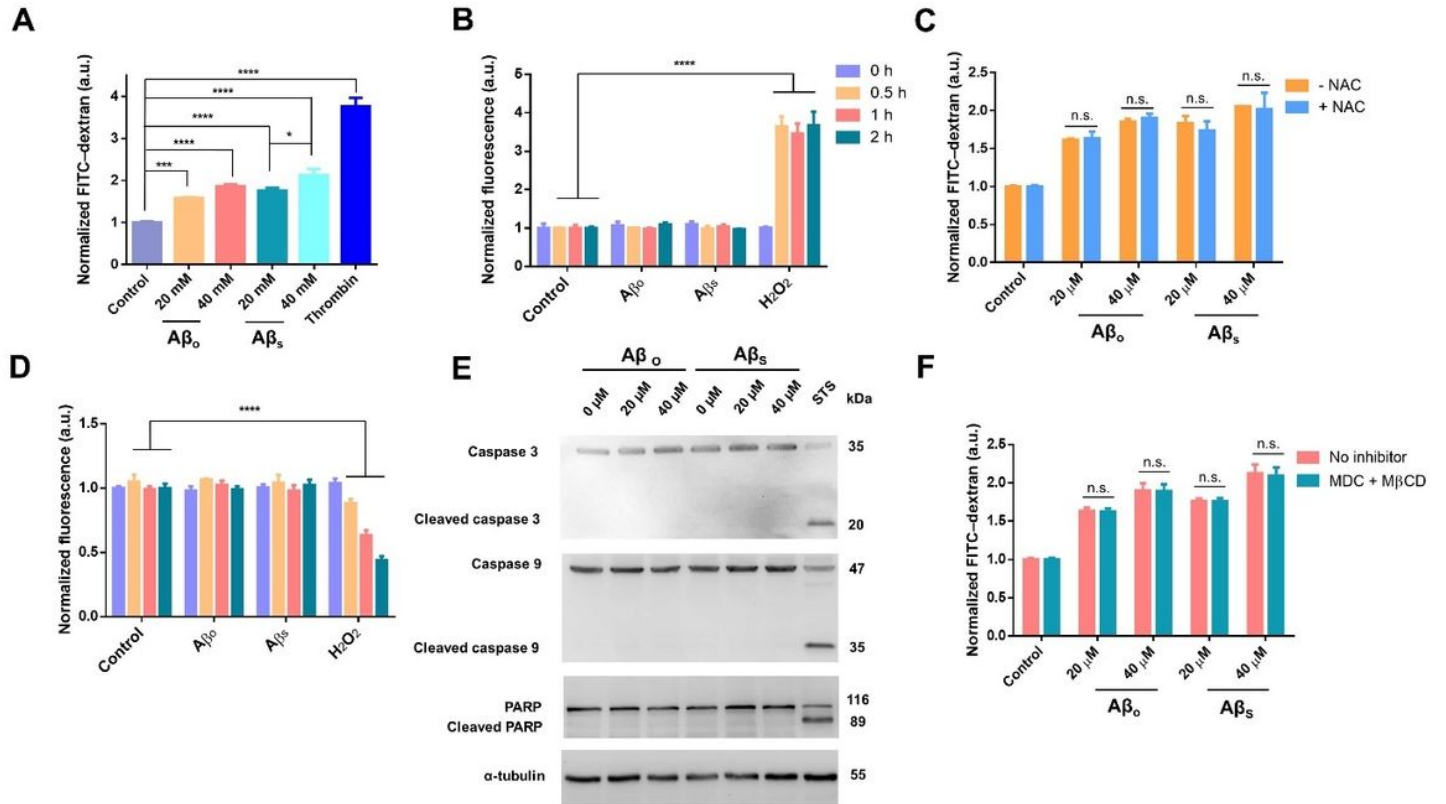


Figure 3

A β -induced APEL is independent of increase in ROS production, decrease in cell viability, apoptotic activation, or endocytosis. **(A)** Treatment of HMVECs with $\text{A}\beta_o$ and $\text{A}\beta_s$ (20 μ M and 40 μ M, 30 min) revealed increases in leakiness with increased concentration of both peptides. Thrombin (3 U/mL) was used as a positive control of induced leakiness. **(B)** No significant increase in ROS production was detected in HMVECs after treatment with different $\text{A}\beta$ ($\text{A}\beta_o$ or $\text{A}\beta_s$, 20 μ M) for as late as 2 h. Hydrogen peroxide (H_2O_2 , 200 μ M) was used as a positive control. **(C)** Induced leakiness from $\text{A}\beta$ APEL treatments was not significantly reduced with prior treatment of ROS scavenger NAC (10 mM, 1 h), when compared to counterparts without NAC treatment. **(D)** No decline in cell viability was detected in HMVECs after treatment with different $\text{A}\beta$ proteins ($\text{A}\beta_o$ or $\text{A}\beta_s$, 20 μ M) for as late as 2 h. **(E)** Immunoblotting with apoptotic markers revealed no activation of apoptosis within concentrations employed in studying $\text{A}\beta$ APEL. Staurosporine (STS; 1 μ M, 2 h) served as positive control for inducing apoptosis. **(F)** Inhibition of endocytosis in HMVECs did not result in a significant reduction in induced leakiness by $\text{A}\beta$ treatments,

when compared against counterparts without inhibitor treatment (mixture of 5 mM M β CD and 10 μ M MDC, from 1 h prior). Results shown as mean \pm SD (n=3), analyzed via two-way ANOVA with Tukey's multiple comparison tests in GraphPad Prism 8. * represents P < 0.05, ** represents P < 0.01, *** represents P < 0.001 and **** represents P < 0.0001 statistical significance. "n.s." represents no statistical significance.

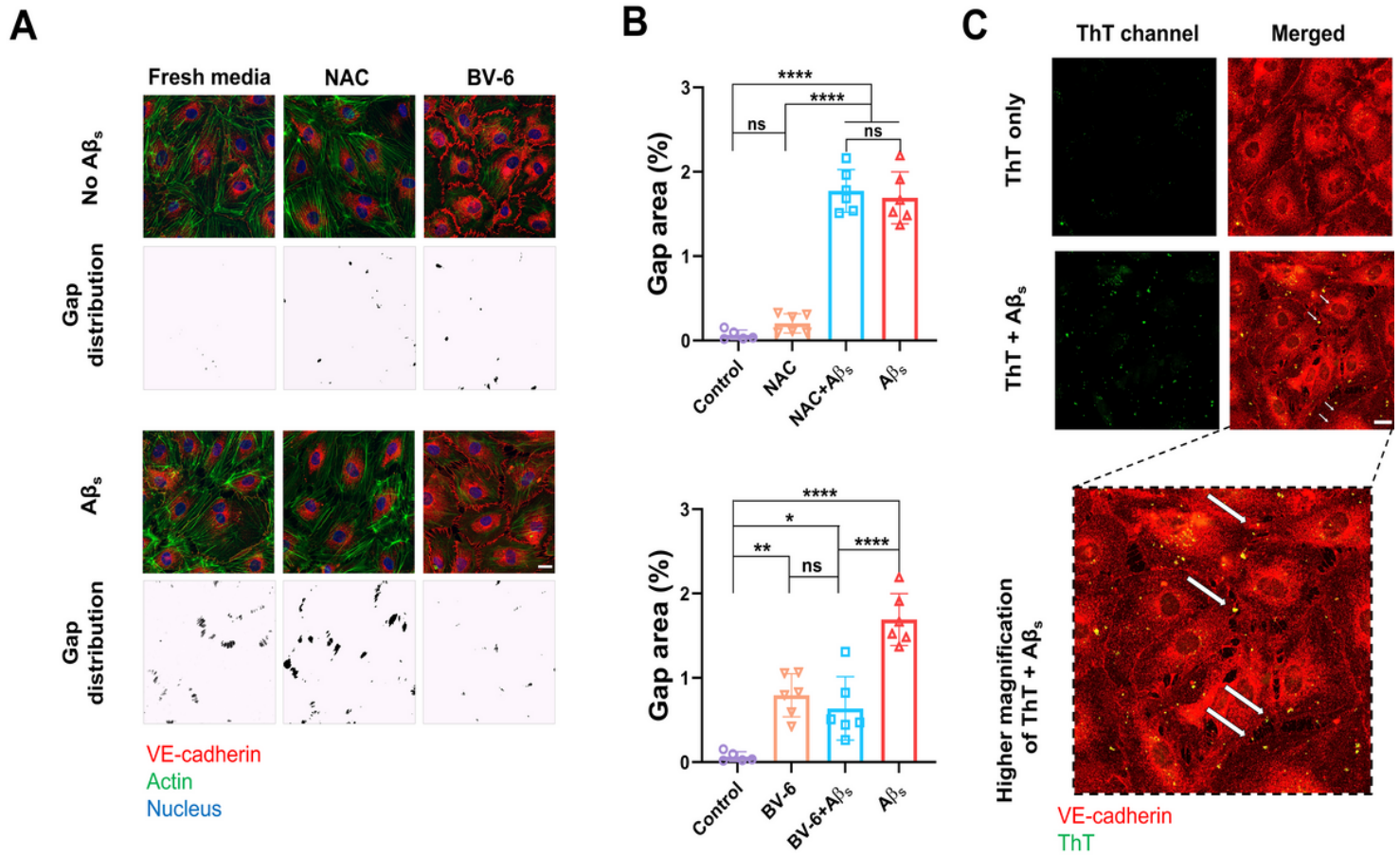


Figure 4

Extracellular interactions with VE-cadherin is necessary for $\text{A}\beta$ APEL induction. **(A)** APEL arising from $\text{A}\beta_s$ (20 μM , 30 min) was inhibited by a BV-6 antibody pre-treatment (dilution 1:100, 1 h prior to amyloid proteins treatment), which specifically blocked the extracellular domain of VE-cadherin. In contrast, no significant reduction in leakiness (gap formation) was observed after $\text{A}\beta_s$ treatment, with or without NAC (10 mM, 1 h pre-treatment). Gap distributions were obtained from captured confocal images through trainable Weka segmentation plugin in ImageJ software. Scale bar = 20 μm . Red: VE-cadherin, green: actin. Y and X axes revealed the combination of pre-treatment (fresh media/NAC/BV-6) and $\text{A}\beta_s$ (-/+). **(B)** Gap area percentages were analyzed by ImageJ according to the images from panel in A. Data are shown as mean \pm SD (n=3), analyzed via one-way ANOVA using GraphPad Prism 8, *represents P < 0.5, ** represents P < 0.01, *** represents P < 0.001 and **** represents P < 0.0001 between the

compared groups. **(C)** Co-localization of ThT-labeled A β _s and VE-cadherin was observed in HMVECs near their cell junctions, revealing association between them. Red: VE-cadherin, green: ThT-labeled A β _s. Scale bar: 20 μ m.

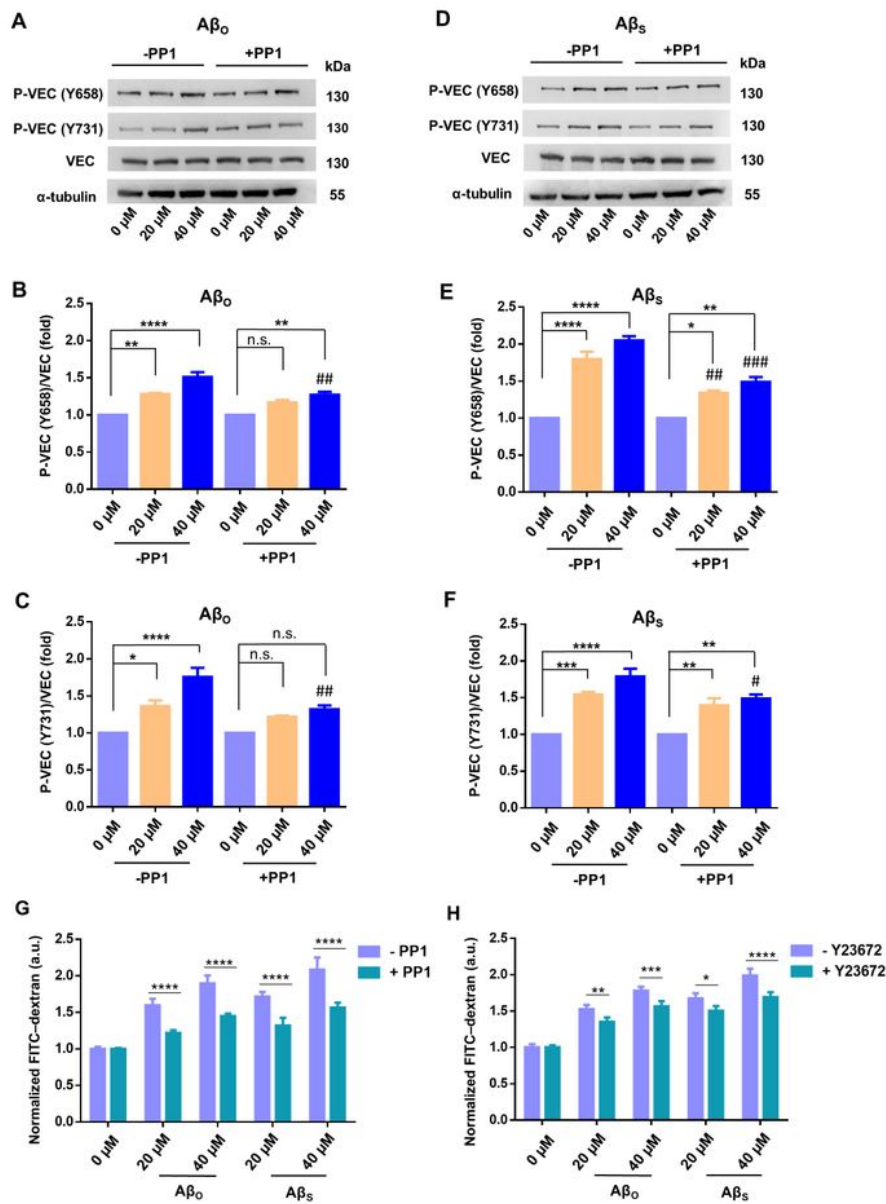


Figure 5

A β -induced APEL involves VE-cadherin signaling and actin remodeling. (A-C) A β _o treatment on HMVECs (20 μ M, 40 μ M) induced activation of VE-cadherin (VEC) signaling, including its phosphorylation at tyrosine residues of 658 (P-VEC(Y658)) and 731 (P-VEC(Y731)). Pre-treatment with Src kinase inhibitor, PP1 (10 μ M, 1 h), led to attenuated activation of these residues. **(D-F)** Similarly, immunoblotting and corresponding semi-quantitative analysis of A β _s treatment revealed activation of VEC signaling, with reduced activation under PP1 pre-treatment. Data are mean \pm SD, n=3 (biologically independent samples, representative blots presented here), analyzed via two-way ANOVA with Tukey's multiple comparison tests. * represents P < 0.05, ** represents P < 0.01, *** represents P < 0.001 and **** represents P < 0.0001 statistical significance. Referring to comparisons between groups with PP1 against their counterparts without PP1, # represents P < 0.05, ## represents P < 0.01, ### represents P < 0.001. "n.s." represents no statistical significance. **(G)** Transwell assay affirmed the significant reduction of A β APEL (A β _o or A β _s, 30 min) due to pre-treatment with PP1 (10 μ M, 1 h), when compared to respective counterparts without PP1. **(H)** A β APEL involved actin remodeling. Pre-treatment with a RhoA kinase (ROCK) inhibitor, Y27632 (10 μ M, 1 h) led to significantly decreased leakiness under A β _o and A β _s (30 min). Results presented are shown as mean \pm SD (n=3), analyzed via two-way ANOVA with Tukey's multiple comparison tests. * represents P < 0.05, ** represents P < 0.01 *** represents P < 0.001 and **** represents P < 0.0001 statistical significance.

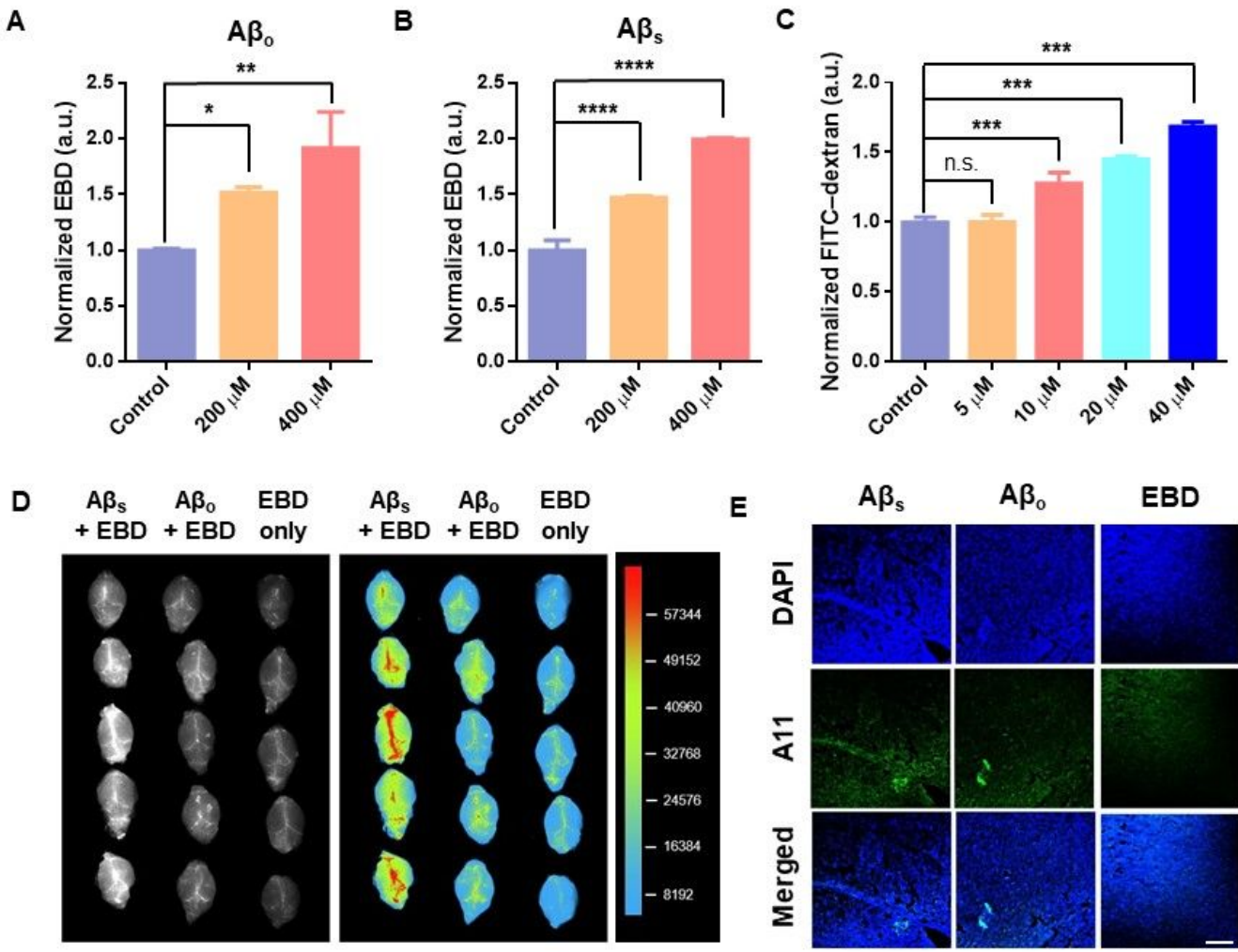


Figure 6

Ex vivo characterization and *in vitro* and *in vivo* blood-brain barrier models of A β -induced endothelial and vascular leakiness. Induced leakiness was observed in swine vessels under the exposure of (A) A β_0 and (B) A β_s . The *ex vivo* penetration of Evans blue dye (EBD) in swine vessels was directly relational to the concentration of A β species (0, 200 and 400 μM). (C) Transwell assay on hCMEC/D3 brain endothelial cells treated with A β_s revealed increased leakiness with increased concentrations. hCMEC/D3 were exposed to A β_s from 0-40 μM , for the duration of 30 min. Penetration of FITC-dextran was used to measure permeability across cells. Results are presented as mean \pm SD (n=3), analyzed via two-way ANOVA with Tukey's multiple comparison tests. * represents P < 0.05, ** represents P < 0.01 *** represents P < 0.001 and **** represents P < 0.0001 statistical significance. (D) *In vivo* experiment involving injection of A β_s or A β_0 (100 μg) into mice revealed the increased leakiness across the blood-brain barrier through measurement of EBD's permeabilization 24 h post-injection. (E) Immunofluorescence analysis of transverse brain sections of mice 24 h post-injection with A β_s or A β_0 (100 μg) revealed presence of A β_0 ,

compared to absence of such structures in brains of mice injected with only EBD. Anti-A11 antibody staining in green and DAPI in blue, with scale bars = 200 μ m.

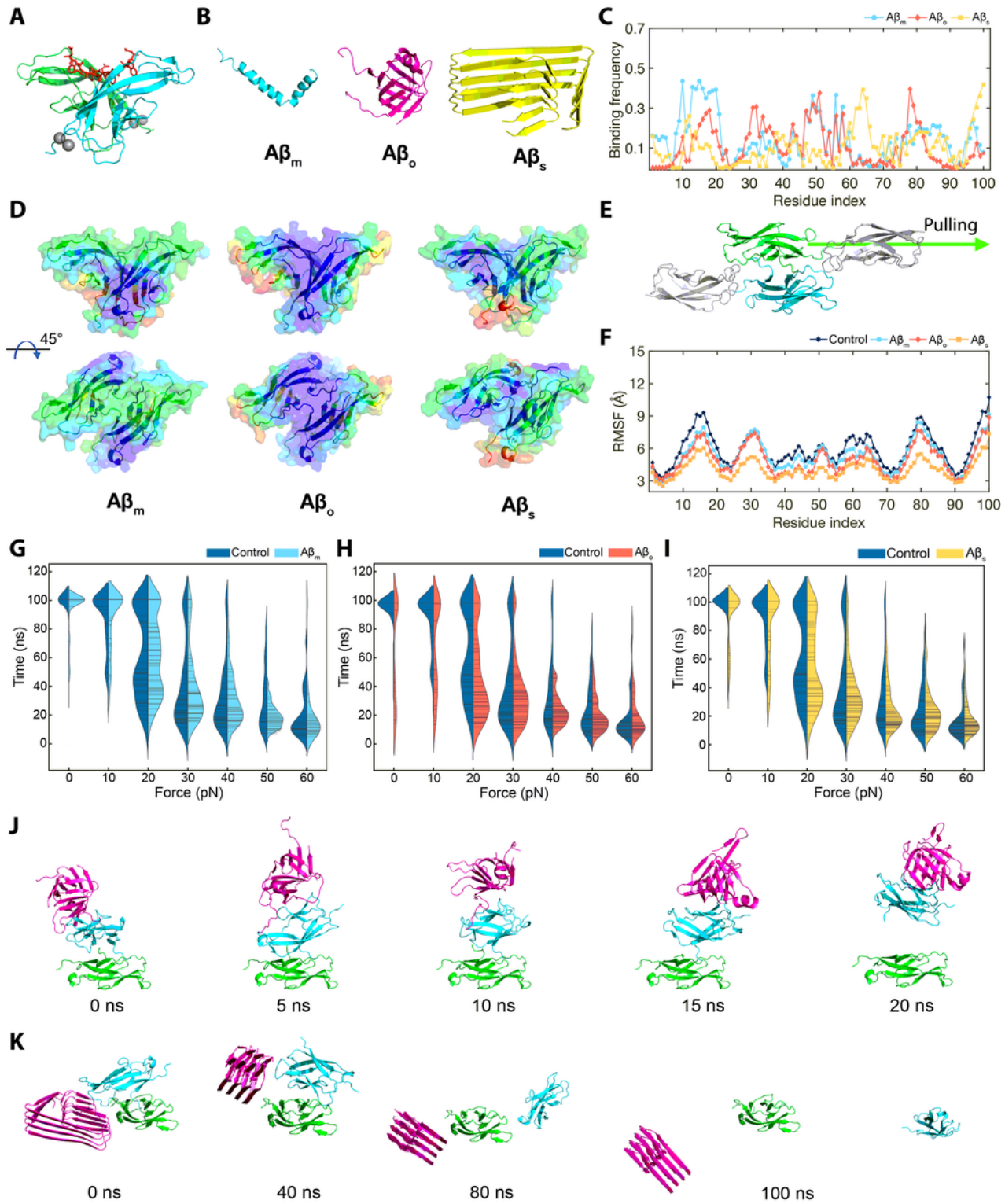


Figure 7

DMD simulations of the binding between A β species and an EC1 cadherin dimer, and sDMD simulations of the cadherin-A β complexes to characterize A β -induced endothelial leakiness. (A) Structure of a EC1 cadherin dimer from the full-length of vascular endothelial cadherin (VE-cadherin). Gray spheres and red sticks represent calcium ions and the domain-swapped region, respectively. (B) Structures of a full-length A β monomer (A β _m), oligomer (A β _o), and seed (A β _s). (C) Binding frequency of the A β species with the EC1 cadherin dimer from the last 10 ns of the binding simulations. (D) Colored binding frequency of the A β species with the EC1 cadherin dimer. Blue and red colors on the EC1 dimer surface indicate low to high binding frequencies. (E) Schematic of steered molecular dynamics (sDMD) simulation employed for this study. (F) Root mean square fluctuation (RMSF) of the EC1 cadherin dimer with and without the A β species. Violin plots for sDMD simulations of the EC1 dimer in the presence and absence of the (G) A β _m, (H) A β _o, and (I) A β _s. Representative dissociation trajectories of the EC1 cadherin dimer with (J) A β _o and (K) A β _s.

Supplementary Files

This is a list of supplementary files associated with this preprint. Click to download.

- [APELSIFinal.docx](#)